

# A Control System for a Microgravity Isolation Mount

Dewi I. Jones, *Member, IEEE*, A. R. Owens, and R. Gareth Owen

**Abstract**—This paper describes the development of a control system and associated technology for a microgravity isolation mount (MGIM)—a device to isolate sensitive scientific payloads on orbiting spacecraft from ambient vibration. The construction of the MGIM, and the specifications which it must satisfy, are briefly described; the control system which achieves this is described in more detail. A model for the MGIM is derived which includes the effect of asymmetric distribution of the payload mass. It is shown that this induces angular motion of the payload and violation of the tolerable microgravity level, unless counteracting control forces are produced. The technology required to support the concept is also described and the results of vibration tests conducted on a full-scale laboratory version of the MGIM are presented.

## I. INTRODUCTION

A major theme of the programs run by the National Aeronautics and Space Administration (NASA) and the European Space Agency (ESA) is the exploitation of the “weightless” condition on orbiting spacecraft for performing experiments in fundamental science. One recent example was the International Microgravity Laboratory (IML-1), a facility dedicated to fundamental materials and life sciences research in earth orbit, which completed a nine-day mission on the space shuttle Discovery in January 1992. Similarly, in April 1993, the European Spacelab was launched on board the space shuttle Columbia carrying a variety of scientific and technological experiments. In the unique environment offered by an orbiting spacecraft, gravity-related effects such as convection, buoyancy, and sedimentation all but disappear, which gives the scientist an opportunity to make observations and measurements which are impossible on earth. It is expected that microgravity experiments will be an important element of the scientific program for the International Space Station.

Elementary dynamics tells us that the “weightless” condition is due to a balance between the centrifugal force on an orbiting object and the force due to the earth’s gravitational field. In practice, there are a number of effects which disturb this balance, and an experimental package fixed inside a spacecraft will typically be subject to small, varying accelerations of  $1\text{--}1000 \mu g$  (where  $g = 9.81 \text{ ms}^{-2}$ ) in magnitude. The standard, though imprecise, term for this condition is microgravity (the true gravitational acceleration in low earth orbit being only slightly less than at the earth’s surface). Despite their small magnitude, these accelerations are sufficient to prejudice some of the extremely sensitive experiments planned for future

Manuscript received July 6, 1994; revised February 6, 1996. Recommended by Associate Editor, M. Spong. This work was supported by European Space Agency Contract 7637/88.

The authors are with the School of Electronic Engineering and Computer Systems, University of Wales, Bangor, Gwynedd LL57 1UT, UK.

Publisher Item Identifier S 1063-6536(96)04922-6.

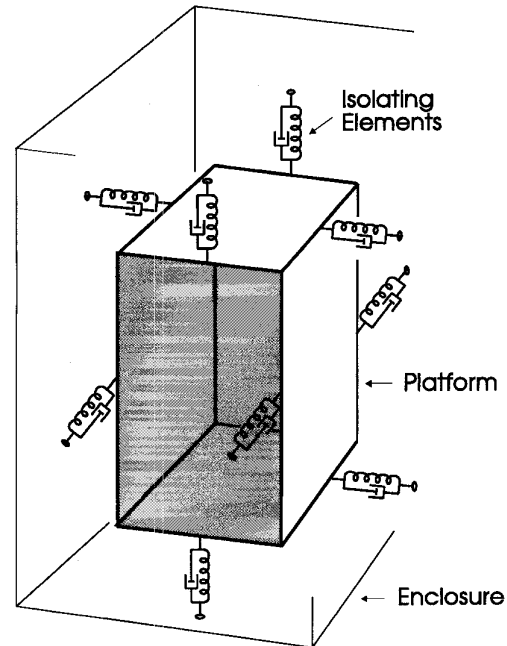


Fig. 1. The principle of platform vibration isolation; in the MGIM the isolating elements are active devices.

missions and it is essential that the vibration at the payload interface is strictly controlled.

Several approaches can contribute to controlling the vibration environment [1]. These range from detailed component design, such as the use of magnetic bearings to attenuate vibration from high-speed rotating devices, through active damping of flexible structures to precision control of whole spacecraft [2]. In this paper we consider only vibration isolation at the payload interface by means of an active suspension system, illustrated conceptually in Fig. 1. The experimental payloads are mounted on the platform which, in practice, is accommodated within a standard spacecraft rack. The isolation elements are actuators and sensors located around the platform to control its motion in six degrees of freedom (DOF's). Long term, the controller ensures that the platform remains central within its enclosure but is isolated from short-term disturbances of the spacecraft structure.

Section II of this paper discusses various sources of microgravity disturbance. Frequency dependent specifications for ambient spacecraft vibration and acceptable microgravity levels for experimental payloads are presented, from which the required microgravity isolation mount (MGIM) transmissibility is derived. A comparison of control strategies, explaining why a noncontact approach was adopted, is given

in Section III. This is followed by a brief description of the MGIM's mechanical design and the technology required for the noncontact transmission of data and electrical power and for platform heat dissipation. A six-DOF model of the MGIM is described in Section IV and the isolation characteristics are predicted. A three-DOF laboratory rig which was used to test the control system and the noncontact technology is described in Section V. The vibration isolation tests confirm the validity of the approach but also demonstrate the difficulties involved in performing such sensitive measurements.

## II. MICROGRAVITY DISTURBANCE SOURCES AND ISOLATION SPECIFICATION

### A. Disturbance Sources

Any payload located within a spacecraft is subject to small accelerations deriving from a number of sources. Because an exact balance between centrifugal force and the earth's gravity exists only at the spacecraft's center of mass, payloads situated away from this point experience a small, quasi-static acceleration known as "gravity-gradient." For an orbital height of 500 km, the magnitude of this acceleration [3] on a payload situated 3 m away from the spacecraft center of mass is about  $1 \mu\text{g}$ . Another component of acceleration, of similar magnitude, exists due to atmospheric drag [3] imparting a small force on the spacecraft's hull along the velocity vector of its center of mass.

Other disturbances originate on the spacecraft itself with contributions from pumps and machinery, the attitude and orbital control system (AOCS), and the oscillation of solar arrays. These sources produce periodic, impulsive, or random accelerations spread across a wide frequency range and with varying magnitude. A serious source of disturbance is the astronauts' movements. Astronauts exercise vigorously during missions to minimize bone and muscle deterioration and this takes place close to operational equipment. The reaction forces propagate through the spacecraft structure. The aggregate of disturbances from all sources is commonly referred to as "g-jitter" and it is particularly undesirable in the 0.01 Hz to 1 Hz frequency range.

### B. Isolation Requirements

The primary requirement which drives the development of the vibration isolation technology is the transmissibility specification. This is based on the magnitude and frequency range of:

- the spacecraft ambient disturbances and
- the desired platform microgravity level.

When this work started in 1985, there was very little data available on the level of acceleration on board the space shuttle and none within the 0.01 Hz to 1 Hz frequency range of interest in this application. Working from the limited accelerometer measurements taken during the SL-1 mission [4] in 1983 and predictions from basic spacecraft models, curve *A* in Fig. 2 was adopted as the envelope of ambient disturbances. Recent measurements made on a space shuttle Atlantis flight using the Honeywell in-space accelerometer

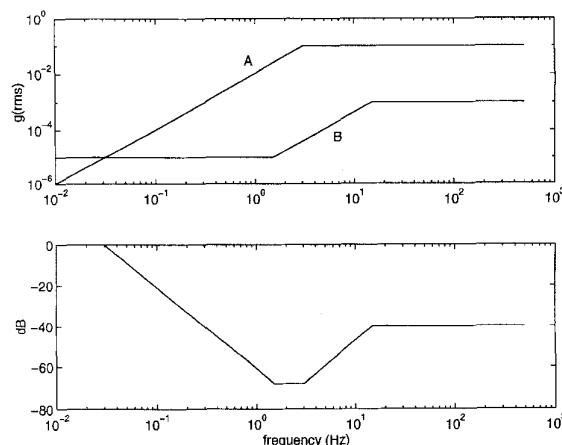


Fig. 2. Sinusoidal specification of acceleration.

have tended to confirm this specification [5]. During this mission a sensitive tri-axial accelerometer package with better than  $1 \mu\text{g}$  resolution and a frequency response down to 0.025 Hz was used to collect data on the shuttle's mid-deck acceleration. It was found that typical background acceleration levels were in the 30–300  $\mu\text{g}$  range, increasing to 650–5000  $\mu\text{g}$  during periods of crew exercise on the treadmill. Peak treadmill events of almost  $10^{-2}\text{g}$  were recorded. Similarly, measurements on microgravity experiment apparatus (e.g., sample change mechanisms, tape recorders) and spacecraft system components (e.g., momentum wheels) showed that they lie within the envelope of curve *A*.

In the early 1980's, a number of theoretical studies were undertaken in an attempt to establish how low the platform microgravity level should be set. Early work, such as that by Tiby and Langbein [6] indicated that a constant level of  $10^{-5}\text{g}$  at low frequencies, relaxing with a square law dependency at high frequencies, would be satisfactory for many potential payloads. Taking this and other studies [7] into consideration, curve *B* in Fig. 2 was adopted as the desired level of platform acceleration.

Combining curves *A* and *B* yields the transmissibility function, curve *C*, which shows that the system must isolate at  $-40 \text{ dB/decade}$  up to 1.5 Hz. Below 0.03 Hz it is permissible for the platform to track the spacecraft; in fact, this is required to limit the differential movement between the platform and its enclosure.

## III. CONTROL STRATEGIES AND DESCRIPTION OF MGIM DESIGN

### A. Approaches to Microgravity Vibration Isolation

Ideally, a microgravity payload's orbit should be determined entirely by the balance between gravitational and centrifugal forces. This can be achieved by regarding the payload as a proof mass and activating thrusters on the spacecraft which force it to follow the proof mass without touching it. Using this principle, von Bun and Garriott [8] have proposed an isolation table which floats freely inside the orbiting laboratory. If the initial release conditions are precisely controlled, it is

estimated that nano- $g$  levels may be achieved for periods of 3000–5000 s, which may be extended to several hours by flying the spacecraft around the table. While this method may achieve an extremely low- $g$  environment, however, the constraints placed on astronaut movement by the free flying table, and the need to integrate the shuttle's AOCSS with an individual payload's control system, inhibit its practicality.

Another approach is to use an unmanned satellite. The European retrievable carrier (EURECA) was launched in July 1992 on a nine-month mission and, as part of its payload, had microgravity experiments to determine how low-gravity conditions affect a variety of organisms, such as spores and fungi. The advantages of this approach are the relatively low cost (compared to manned missions) and long-duration high-quality microgravity. Set against this is the absence of flexibility in experiment operation and interactive working offered by a manned laboratory.

The approach investigated here is to provide vibration isolation at the payload interface within a manned spacecraft, as indicated in Fig. 1. The ambient spacecraft rms sinusoidal vibration amplitude is given by the +40 dB/decade asymptote of curve *A*, Fig. 2, as

$$x_{\text{rms}} = \frac{\ddot{x}_{\text{rms}}}{(2\pi f)^2}. \quad (1)$$

For the range of “ $g$ ” values in curve *A*, this evaluates to  $x_{\text{rms}} = 2.76$  mm corresponding to a peak of 3.9 mm. Allowing some margin, the isolating elements must operate over a  $\pm 7$  mm range. Their stiffness ( $K$ ) is given by

$$K = (2\pi f_o)^2 M \quad (2)$$

where  $M$  is the platform mass and  $f_o$  is the break frequency. For typical values of  $M = 100$  kg and  $f_o = 0.03$  Hz, this gives a stiffness of about 3 N/m—a very soft spring, which would be difficult to realize mechanically.

Ideally, the payload is located near to the spacecraft's center of mass, to minimize quasi-static effects. When the payload is located away from the spacecraft's center of mass, rotation of the spacecraft appears as both a translational and rotational component of acceleration at the payload site. The relative importance of the two components is determined approximately by the ratio of the distance of the platform from the spacecraft center of mass to the distance of the platform's periphery from its own center of mass. In our case, this ratio is assumed to be sufficiently large for the translational component to be dominant. It is required that the vibration isolation be effective in the three rectilinear DOF's, so isolating elements which act along one axis must allow free motion in the other directions. Elements acting in the same direction must be well matched in their elastic and damping characteristics as any mismatch will induce angular rotation of the platform. The match must be maintained despite changes in environmental conditions and aging. Because the platform will accommodate various payloads, the isolation elements must compensate for changes in the mass and moment of inertia and any offset of the payload center of mass from the center of geometry.

The above requirements indicate that an actively controlled suspension system is preferable. As other studies have shown

[9], [10], its adaptability and superior performance are decisive factors in its favor despite the penalty of increased complexity, power requirement and weight.

### B. Control Strategies

There are two basic methods for actively controlling the platform. One option is to connect the platform to its enclosure by means of a physical umbilical. The umbilical's natural compliance will transmit vibration to the platform which must then be rejected (i.e., counteracting forces must be exerted). Alternatively, the platform may be allowed to float freely with no physical contact, thus isolating it from ambient vibration, and relying on its own mass to provide the required inertial reference. In this case a highly compliant “noncontact umbilical” must be developed to supply payload services.

Several systems based on the first option have been proposed. Fenn *et al.* [11] and Germann and Gupta [12] have investigated the use of acceleration feedback, the accelerometers being mounted upon the platform, and used to generate control forces by means of an electromagnetic actuator of the Lorentz force type. Grodsinsky and Logsdon [13] have investigated the use of relative position sensors, and accelerometers mounted on the enclosure, to generate an absolute platform velocity signal for control purposes. Stampleman and von Flotow [14] have proposed a hybrid scheme based on piezoelectric film springs giving passive isolation which is then enhanced by active acceleration feedback to provide the required rejection forces. A system based upon a Stewart platform with high bandwidth, high force magnetostrictive linear actuators, and force and acceleration sensing has recently been described by Geng and Haynes [15]. The advantage of this first option is that a physical umbilical makes it easy to provide platform services by means of electrical cable banding and a water cooling loop. An investigation of control strategies [16], however, has revealed that the umbilical itself introduces difficulties:

- The umbilical must be as compliant as possible, but sufficiently stiff to retain its shape so that there is no danger of “snagging” on nearby components; a stiffness of at least 20 N/m is required [14].
- A fluid cooling loop produces a significant disturbance due to momentum transfer [11].
- A higher bandwidth control loop is required resulting in larger actuators and increased power consumption.
- A high grade accelerometer is required which can resolve down to 1  $\mu g$  at low frequencies and which must possess a very low temperature coefficient of bias.
- The accelerometer package consumes payload volume.

As in FEAMIS (fluid experiment apparatus magnetic isolation system) described by Allen *et al.* [17], the MGIM does not use accelerometers. Whereas the 3 Hz bandwidth of FEAMIS allows a physical umbilical to be used, however, our method is entirely “noncontact.”

### C. Description of the MGIM

Fig. 3 shows that the mechanical construction [18], [19] is in two parts, consisting of a liner unit which tailors the inside of the spacecraft's standard rack to this application

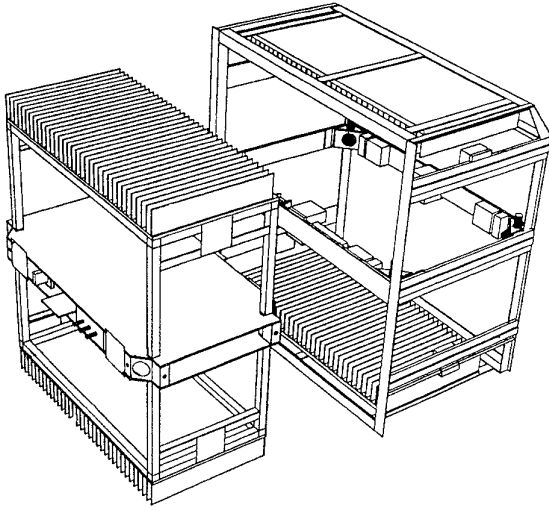


Fig. 3. Outline mechanical structure of the microgravity isolation mount.

and the platform unit which is the isolated element holding the experimental payload. The platform unit slides inside the liner unit where it is controlled by the sensor/actuator units (SAU). A locking mechanism captures the platform during nonoperational periods and provides firm restraint during launch and landing.

The services to the platform consist of:

- **Electrical Power:** Payload studies have revealed that some materials science experiments, such as the advanced gradient heating facility, require considerable amounts of electrical power (1–3 KW) for heating furnaces. Electrical power is transmitted by means of a transformer with a loosely coupled secondary. A prototype unit has demonstrated transmission of 1 kW across a 7 mm gap with better than 90% efficiency [20] and negligible disturbance forces.
- **Cooling:** Heat dissipated on the platform must be returned to the spacecraft's cooling subsystem which is available in the form of a cooled water supply at each rack. About three quarters of the thermal dissipation is by means of radiation with conduction through the air in the gap accounting for the remainder. As shown in Fig. 3, the platform is clad with cooling fins which interlace with another set of fins mounted on water cooled panels inside the liner [20].
- **Data and Control Signal Transmission:** Low data rate channels are needed so that the payload specialist may interact with the experiment and high data rate channels (25 Mb/s) give video signal transmission. Data transmission across the platform/liner gap is by means of an infrared optical link [20].

The SAU's, shown in Fig. 4, are also noncontact. Essentially the actuators consist of coils with low-hysteresis cores located on the liner which are excited to attract target plates fixed on the platform [21]. They are arranged in pairs along a line of action and, when driven with appropriate linearization and switching circuitry, allow control of the

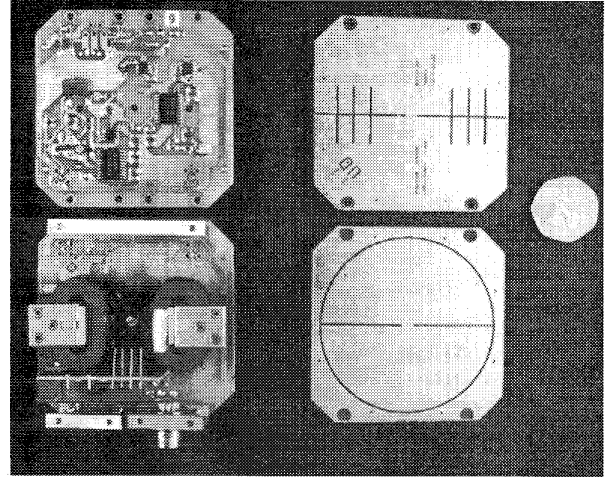


Fig. 4. Photograph of SAU before assembly; top left—sensor drive circuit, bottom left—actuator coil, bottom right—capacitance sensor plate.

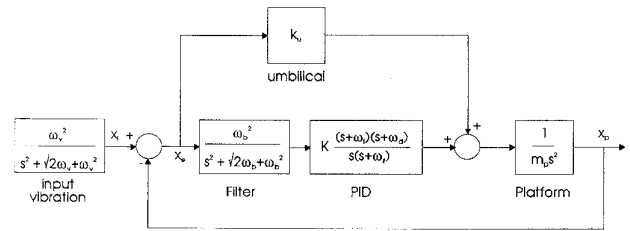


Fig. 5. Basic single axis control loop.

forces and moments exerted on the platform. Differential capacitance sensors, which are collocated with the actuators, measure the relative displacement between platform and liner [21]. The rectilinear displacement along any axis is given by the mean signal of a pair of sensors while the difference signal gives a measure of rotation.

#### IV. CONTROL METHODS

##### A. Single-Axis Controller

Provided the platform is completely free, the transmissibility of curve *C* in Fig. 2 is obtained by means of conventional proportional integral derivative (PID) control applied to a measurement of the platform/liner gap. This is shown in Fig. 5 where:

- $\omega_v$  break frequency of input vibration (3 Hz);
- $\omega_b$  break frequency of filter (0.2 Hz);
- $k_u$  umbilical stiffness;
- $K$  loop gain;
- $\omega_i$  break frequency of integral term (0.001 47 r/s);
- $\omega_d$  break frequency of derivative term (0.118 r/s);
- $\omega_l$  break frequency of lag term (0.377 r/s);
- $m_p$  platform mass (150 kg).

The filter is included in the forward loop to limit force transmission at high frequency and the integral term counteracts the quasi-static disturbances.

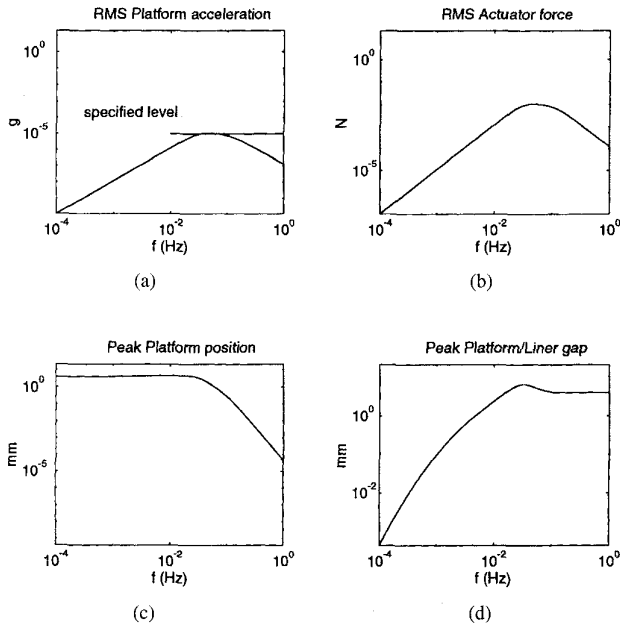


Fig. 6. Nominal frequency responses for the single-axis controller.

Fig. 6(a) shows that the platform acceleration complies with the acceleration specification and Fig. 6(b) that the actuator force required to achieve this is of the order of 0.01 N. Fig. 6(c) shows that the peak platform displacement is 4.5 mm compared with the peak liner displacement of 3.9 mm (see Section III-A). Fig. 6(d) shows that the peak relative displacement is 6.3 mm, which is within the allowed 7 mm gap between the platform and liner.

The integral term in the controller counteracts quasi-static disturbances. Gravity gradient produces a constant acceleration,  $g_g$ , acting radially toward the earth in the plane of the orbit; a similar component occurs due to any displacement out of the plane of the orbit. Unless counteracted, it will cause the platform to move from its mean central position within the liner. Its magnitude is [3]

$$g_g = 2 \left( \frac{\omega_0^2}{9.81} \right) \quad (3)$$

per meter of displacement of the payload away from the spacecraft center of mass, where  $\omega_0$  is the orbital rate. In low earth orbit this evaluates to approximately  $3 \times 10^{-7}$  g/m. Fig. 7 shows the platform's initial release response to gravity gradient assuming the MGIM is 1 m away from the spacecraft's center of mass. The maximum displacement is 1.6 mm which reduces to zero as the integral term in the controller takes effect.

The effects of atmospheric drag vary with orbital height, spacecraft orientation and solar activity. For a 450 km orbit, Sharpe [7] presents a drag profile over one orbit which varies between  $2 \times 10^{-8}$  g (night) to  $6 \times 10^{-7}$  g (day). Using this profile as an input acceleration, the resultant platform displacement is shown in Fig. 7 to be limited by integral action to within about 2 mm of its central position.

### B. Geometry of the MGIM

Fig. 8 shows two reference frames:  $O'x'y'z'$ , which is fixed to the liner and has its origin at the geometric center, and

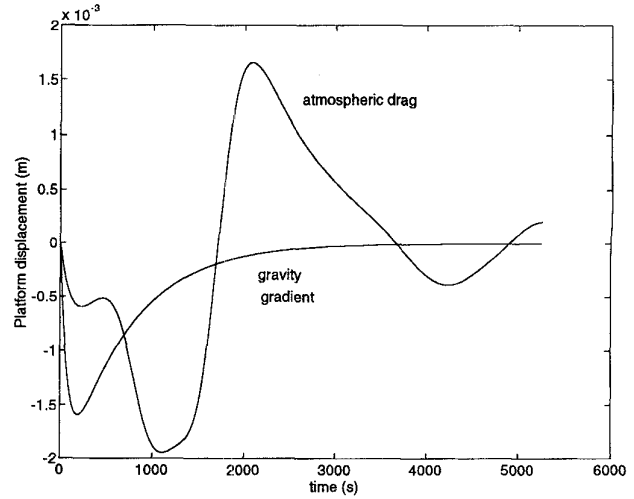


Fig. 7. Transient displacement of platform due to quasi-static disturbances.

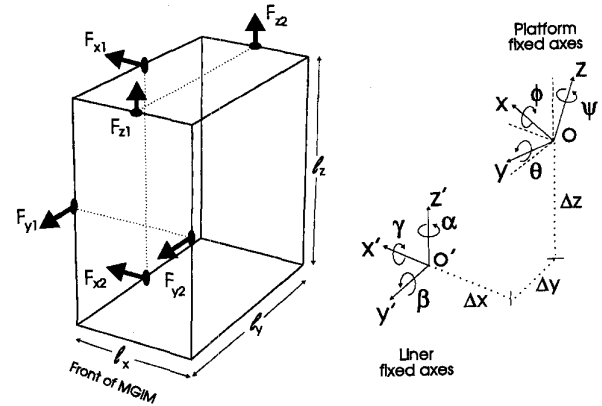


Fig. 8. Coordinate reference frames and lines of action of actuator forces on MGIM platform (only 1/2 of each SAU pair is shown).

$Oxyz$ , which is fixed to the platform and has its origin at the platform's center of mass and is aligned with its principal inertia axes. The convention used for  $O'x'y'z'$  is the Spacelab coordinate system [22] which is based on the orbiter structural body coordinate system and has the positive  $x$ -axis in the direction of the tail, the positive  $z$ -axis up, and the positive  $y$ -axis in the direction of the right wing. The origin of  $Oxyz$  is displaced from the origin of  $O'x'y'z'$  by  $\Delta x$ ,  $\Delta y$  and  $\Delta z$ , respectively, and the axes rotated by the roll, pitch, and yaw angles  $\gamma$ ,  $\beta$ , and  $\alpha$ , respectively.

If the platform has a symmetric mass distribution then its center of mass ( $O$ ) coincides with its center of geometry and that of the liner ( $O'$ ). This is generally not the case, however, because placing an experimental package on the platform displaces the center of mass and rotates the principal axes of inertia, as illustrated in Fig. 9(a). For a given mass distribution, the location and orientation of  $Oxyz$  remain substantially constant with respect to  $O'x'y'z'$  (i.e.,  $\Delta x$ ,  $\Delta y$  and  $\Delta z$  and  $\alpha$ ,  $\beta$  and  $\gamma$  are constant) because the vibratory motion of the liner is very small compared to the size of the platform. Moreover, limits on the permissible mass asymmetry

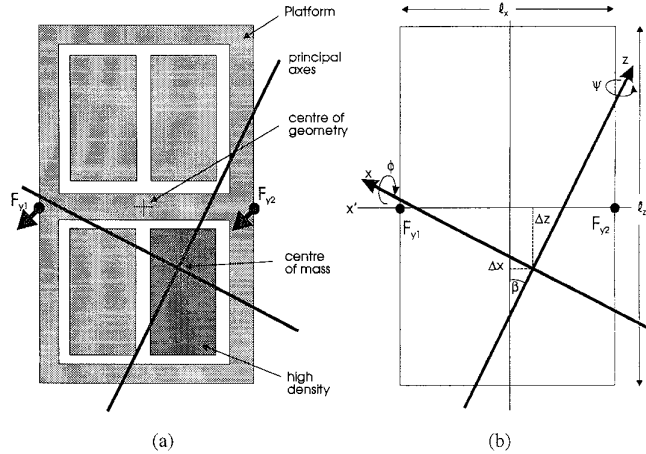


Fig. 9. Displacement of center of mass and rotation of principal axes of inertia due to asymmetric mass distribution.

will be imposed on experimenters' payloads so that in practice  $\Delta x, \Delta y, \Delta z, \alpha, \beta, \gamma$  are small but significant.

The location of the SAU's on the MGIM is such that the line of force for any given set (e.g., the four  $y$ -axis SAU's) passes through the center of geometry of the liner. Fig. 8 shows that the sensors located on the MGIM front measure the gaps  $y_1$  and  $y_2$  between the platform and liner. The actuators, collocated with the sensors, act together to control translation along the  $y$ -axis and differentially to control rotation about the  $z$ -axis. Corresponding units at  $x_1, x_2$  and  $z_1, z_2$  control motion in the  $xz$  and  $yz$  planes, respectively. Any displacement of the center of mass causes the actuators to exert a moment on the platform and it is necessary for the control system to suppress the consequent angular motion.

Consider the case shown in Fig. 9(b). The actuators at  $y_1$  and  $y_2$  produce forces parallel to the  $y'$  axis. The total force applied at the center of mass is

$$F_y = F_{y1} + F_{y2}. \quad (4)$$

In general, a pitch or yaw of the principal axes would cross-couple force components from the  $y$  and  $z$  actuators. The coupling is small for the range of principal axes rotation encountered in practice, however, and may be omitted.

Again, inspection of Fig. 9(b) shows that the  $y$  actuators also apply moments  $T_x$  and  $T_z$  about the  $x$  and  $z$  axes, respectively. The moments are given by the product of the actuator force and its perpendicular distance to the axes  $Oxyz$ . Assuming small angle approximations, the following expressions may be deduced:

$$T_z = F_{y1} \left[ \left( \frac{\ell_x}{2} - \Delta x \right) + \Delta z \beta \right] + F_{y2} \left[ - \left( \frac{\ell_x}{2} + \Delta x \right) + \Delta z \beta \right] \quad (5)$$

$$T_x = F_{y1} \left[ \Delta z - \left( \frac{\ell_x}{2} - \Delta x \right) \beta \right] + F_{y2} \left[ \Delta z + \left( \frac{\ell_x}{2} + \Delta x \right) \beta \right]. \quad (6)$$

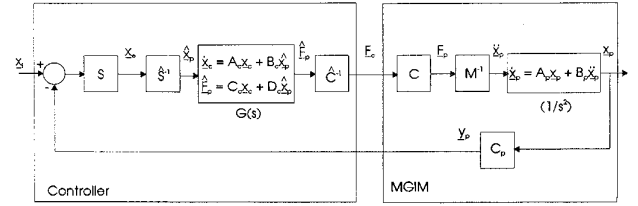


Fig. 10. Six degree of freedom control loop for MGIM.

### C. Six Degree of Freedom Model

A six degree of freedom state-space model based on Fig. 5 and (4)–(6) is shown in Fig. 10. The generalization is straightforward because the angular displacements and velocities are very small and the coupling terms in the Euler equations are negligible.

The dynamic equation for a platform of mass  $m$  and principal moments of inertia  $I_{xx}, I_{yy}$ , and  $I_{zz}$  may be taken as

$$\begin{bmatrix} x \\ y \\ z \\ \phi \\ \theta \\ \psi \end{bmatrix} = \frac{1}{s^2} \begin{bmatrix} 1/m & & & & & \\ & 1/m & & & & \\ & & 1/m & & & \\ & & & 1/m & & \\ & & & & 1/m & \\ & & & & & 1/m \end{bmatrix} \begin{bmatrix} F_x \\ F_y \\ F_z \\ T_x \\ T_y \\ T_z \end{bmatrix} \quad (7)$$

which is of the form

$$\mathbf{x}_p = \frac{1}{s^2} \mathbf{M}^{-1} \mathbf{F}_p \quad (8)$$

where:

- $s$  is the Laplace transform variable;
- $\mathbf{F}_p$  is a vector of generalized forces acting on the platform;
- $\mathbf{x}_p$  is the inertially referred vector of generalized platform displacements;
- $\mathbf{M}$  is the platform's mass/inertia matrix.

It should be noted that the reaction force on the spacecraft due to the actuators has been omitted in (7) as its mass is very much larger than that of the platform. Consequently, the motion of the spacecraft (and hence the liner), which results from the combined disturbance forces discussed in Section II-A, is represented by the displacement input,  $\mathbf{x}_s$ , in Fig. 10. Gravity gradient, which acts directly as a disturbance input on the platform, is also omitted from (7) for the purposes of designing a controller in the frequency range of interest.

Referring to (5) and (6), the forces exerted on the platform,  $\mathbf{F}_p$ , are related to the actuator forces,  $\mathbf{F}_c$ , by the actuator configuration matrix,  $\mathbf{C}$  (see (9) shown at the bottom of the next page) which is of the form

$$\mathbf{F}_p = \mathbf{C} \mathbf{F}_c. \quad (10)$$

*Controller:* The measured variable is the relative displacement between liner and platform,  $\mathbf{x}_e$ , which is related to the platform coordinates,  $\mathbf{x}_p$ , by the sensor configuration matrix,  $S$

$$\mathbf{x}_e = S(\mathbf{x}_i - C_p \mathbf{x}_p). \quad (11)$$

where  $C_p$  is an output matrix which selects position information only. For the allowable rotational range of the MGIM platform, the small angle approximation for  $\phi, \theta$  and  $\psi$  is valid and  $S$  is given by (12), shown at the bottom of the next page.

The rectilinear and angular effects can be decoupled by means of the inverse control scheme, also shown in Fig. 10

$$\mathbf{F}_c = \hat{C}^{-1}[G(s)]\hat{S}^{-1}\mathbf{x}_e \quad (13)$$

where:

$\hat{C}^{-1}$  is an estimate of the inverse actuator configuration matrix;

$\hat{S}^{-1}$  is an estimate of the inverse sensor configuration matrix.

In (13),  $[G(s)]$  is a diagonal matrix of PID compensators tuned to the nominal platform mass and principal moments of inertia. The  $\hat{\cdot}$  symbol is used because there may be uncertainty in our knowledge of the position of the center of mass, i.e.,  $\Delta x, \Delta y$ , and  $\Delta z$ , and the orientation of the principal axes, i.e.,  $\alpha, \beta$ , and  $\gamma$ . The matrices  $\hat{C}^{-1}$  and  $\hat{S}^{-1}$  are effectively embedded inverse plant models and are obtained from (10) and (7) using the Matlab symbolic toolbox. Neglecting second order and higher terms in the case of  $\hat{C}^{-1}$ , they are (14) and (15), shown at the bottom of the next page.

To be invertible,  $S$  and  $C$  must be square and nonsingular. The first condition is satisfied as there are always six independently controllable SAU's. The determinants of  $S$  and  $C$  are given by

$$|S| = \ell_x \ell_y \ell_z \quad (16)$$

$$|C| = -\ell_x \ell_y \ell_z (\alpha \beta \gamma - 1) \quad (17)$$

from which it is evident that  $S$  or  $C$  is singular if  $\ell_x, \ell_y$ , or  $\ell_z$  is zero, i.e. if two SAU's acting on the same axis are not physically separated.

#### D. Predicted System Response

Expressions for the platform's acceleration and displacement may be obtained from the model of Fig. 10, as shown in the Appendix. Referring to the three degree of freedom (planar) simplification of Fig. 11, the acceleration at one corner of the platform (a worst case), in the direction specified by angle  $\rho$ , is given by

$$a = \ddot{z} \cos \rho + \ddot{x} \sin \rho + r \ddot{\theta} \sin(\delta - \rho) + r \dot{\theta}^2 \cos(\delta - \rho) \quad (18)$$

where:

$\ddot{x}, \ddot{z}$  are the components of acceleration along the  $x$  and  $z$  axes (see the Appendix);

$r \ddot{\theta}$  is the tangential acceleration;

$r \dot{\theta}^2$  is the centripetal acceleration;

$r, \delta$  are the length and angle, respectively, of a line drawn between the platform corner and the center of mass.

Angles  $\rho$  and  $\delta$  are measured from the platform's principal axis,  $z$ , and  $r$  and  $\delta$  are given by

$$r = \sqrt{\left(\frac{\ell_x}{2} - \Delta x\right)^2 + \left(\frac{\ell_z}{2} - \Delta z\right)^2}$$

$$\delta = \pi + \tan^{-1}\left(\left(\frac{\ell_x}{2} - \Delta x\right) / \left(\frac{\ell_z}{2} - \Delta z\right)\right) - \beta. \quad (19)$$

The inverse controller described previously isolates both translational and rotational input vibration but does depend on knowledge of  $\Delta x, \Delta y, \Delta z, \alpha, \beta$ , and  $\gamma$  (which will be known fairly accurately for a given payload). A more robust approach when (as here) there is no rotational input, however, is to set the angle control loops to a higher bandwidth, to provide angular constraint; this also simplifies the controller [23]. In our case the bandwidth is set at 0.3 Hz—10 times higher than

$$\begin{bmatrix} F_x \\ F_y \\ F_z \\ T_x \\ T_y \\ T_z \end{bmatrix} = \begin{bmatrix} 1 & 1 & 0 \\ 0 & 0 & 1 \\ 0 & 0 & 0 \\ 0 & 0 & \left[\Delta z - \left(\frac{\ell_x}{2} - \Delta x\right)\beta\right] \\ \left[\left(\frac{\ell_z}{2} - \Delta z\right) + \Delta y\gamma\right] & \left[-\left(\frac{\ell_z}{2} + \Delta z\right) + \Delta y\gamma\right] & 0 \\ \left[\Delta y - \left(\frac{\ell_z}{2} - \Delta z\right)\gamma\right] & \left[\Delta y + \left(\frac{\ell_z}{2} + \Delta z\right)\gamma\right] & \left[\left(\frac{\ell_x}{2} - \Delta x\right) + \Delta z\beta\right] \\ 0 & 0 & 0 \\ \left[\Delta z + \left(\frac{\ell_x}{2} + \Delta x\right)\beta\right] & \left[\left(\frac{\ell_y}{2} - \Delta y\right) + \Delta x\alpha\right] & \left[-\left(\frac{\ell_y}{2} + \Delta y\right) + \Delta x\alpha\right] \\ 0 & \left[\Delta x - \left(\frac{\ell_y}{2} - \Delta y\right)\alpha\right] & \left[\Delta x + \left(\frac{\ell_y}{2} + \Delta y\right)\alpha\right] \\ \left[-\left(\frac{\ell_x}{2} + \Delta x\right) + \Delta z\beta\right] & 0 & 0 \end{bmatrix} \cdot \begin{bmatrix} F_{x1} \\ F_{x2} \\ F_{y1} \\ F_{y2} \\ F_{z1} \\ F_{z2} \end{bmatrix} \quad (9)$$

the translational loops. Fig. 12 and Fig. 13 show the predicted accelerometer output, as a function of frequency, as  $\Delta x$  and  $\Delta z$  range from 0–7 cm. The value of  $\rho$  is  $90^\circ$  (almost worst case) and the input motion, in the  $x'$  direction only, conforms to curve *A* in Fig. 2. As expected, the variation of the curves with  $\Delta x$  and  $\Delta z$  is very much less in Fig. 13 because angular motion is being suppressed.

## V. LABORATORY TEST RIG AND RESULT

### A. Description of Test Rig

A full-scale laboratory model of the MGIM was constructed to demonstrate the noncontact technology and to confirm the vibration isolation characteristics. The liner unit is housed

within a standard 19" rack unit, as shown in Fig. 14. The rack unit is supported on slide rails and attached at its midpoint to an electromagnetic shaker via an A frame linkage and can be vibrated along the  $y'$  axis. The platform is fixed to a precision ground plate supported on a custom-made air table, as shown in Fig. 15.

The air table rests on a three-point mounting fixed to a heavy steel plinth on a stable floor. Each mount has a 0.5 mm micrometer screw for levelling the air table. The platform is free to move in the horizontal plane with three DOF's ( $x, y, \psi$ ) up to 7 mm from its central position. Two of the SAU's can be seen at the top and bottom of the platform in Fig. 15. A locking mechanism to clamp the platform to the liner is concealed behind the central belt. The optical data link is the unit to the upper left of the platform while the unit on top

$$S = \begin{bmatrix} 1 & 0 & 0 & 0 & \left(\frac{l_z}{2} - \Delta z\right) & 0 \\ 1 & 0 & 0 & 0 & -\left(\frac{l_z}{2} + \Delta z\right) & 0 \\ 0 & 1 & 0 & 0 & 0 & \left(\frac{l_x}{2} - \Delta x\right) \\ 0 & 1 & 0 & 0 & 0 & -\left(\frac{l_x}{2} + \Delta x\right) \\ 0 & 0 & 1 & \left(\frac{l_y}{2} - \Delta y\right) & 0 & 0 \\ 0 & 0 & 1 & -\left(\frac{l_y}{2} + \Delta y\right) & 0 & 0 \end{bmatrix} \quad (12)$$

$$\hat{S}^{-1} = \begin{bmatrix} \frac{1}{2} + \frac{\Delta z}{l_z} & \frac{1}{2} - \frac{\Delta z}{l_z} & 0 & 0 & 0 & 0 \\ 0 & 0 & \frac{1}{2} + \frac{\Delta x}{l_x} & \frac{1}{2} - \frac{\Delta x}{l_x} & 0 & 0 \\ 0 & 0 & 0 & 0 & \frac{1}{2} + \frac{\Delta y}{l_y} & \frac{1}{2} - \frac{\Delta y}{l_y} \\ 0 & 0 & 0 & 0 & \frac{1}{l_y} & -\frac{1}{l_y} \\ \frac{1}{l_z} & -\frac{1}{l_z} & 0 & 0 & 0 & 0 \\ 0 & 0 & \frac{1}{l_x} & -\frac{1}{l_x} & 0 & 0 \end{bmatrix} \quad (14)$$

$$\hat{C}^{-1} = \begin{bmatrix} \frac{1}{2} + \frac{\Delta z}{l_z} & \frac{-\alpha \Delta z}{l_z} & \frac{-\Delta x}{l_z} & \frac{\alpha}{l_z} & \frac{1}{l_z} & 0 \\ \frac{1}{2} - \frac{\Delta z}{l_z} & \frac{\alpha \Delta z}{l_z} & \frac{\Delta x}{l_z} & \frac{-\alpha}{l_z} & -\frac{1}{l_z} & 0 \\ -\frac{\Delta y}{l_x} & \frac{1}{2} + \frac{\Delta x}{l_x} & \frac{-\Delta x}{l_x} & 0 & \frac{\gamma}{l_x} & \frac{1}{l_x} \\ \frac{\Delta y}{l_x} & \frac{1}{2} - \frac{\Delta x}{l_x} & \frac{\gamma \Delta x}{l_x} & 0 & \frac{\gamma}{l_x} & \frac{l_x}{l_x} \\ \frac{l_x}{\beta \Delta y} & \frac{-\Delta z}{l_x} & \frac{1}{2} + \frac{\Delta y}{l_x} & \frac{1}{l_x} & 0 & \frac{l_x}{\beta} \\ -\frac{l_y}{\beta \Delta y} & \frac{-\Delta z}{l_y} & \frac{1}{2} + \frac{\Delta y}{l_y} & \frac{1}{l_y} & 0 & \frac{l_y}{\beta} \\ \frac{\beta \Delta y}{l_y} & \frac{\Delta z}{l_y} & \frac{1}{2} - \frac{\Delta y}{l_y} & \frac{-1}{l_y} & 0 & -\frac{\beta}{l_y} \end{bmatrix} \quad (15)$$

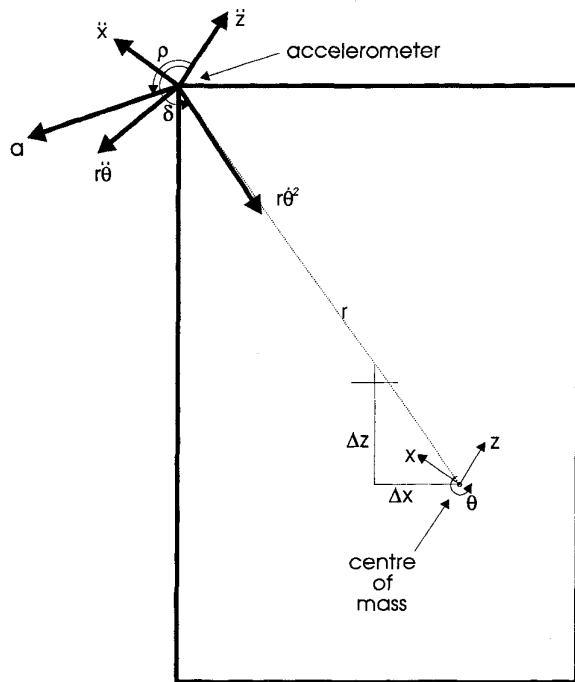


Fig. 11. Acceleration at extremity of platform due to translational and rotational motion.

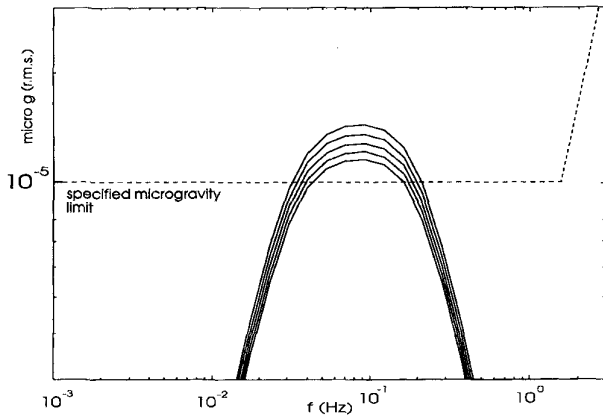


Fig. 12. Predicted acceleration at corner of platform without rotational control.

connects to a wiring loom which is used to transfer power, data and control signals from the control electronics unit to the liner during testing.

**B. Control System Implementation**

The controller is implemented on two INMOS T414 transputers, one running the real-time controller and the other the user interface, as shown in Fig. 16. Communication between the transputers is by means of standard 10 Mb/s serial links. The dynamic control loop is triggered at a sampling rate of 10 ms and executes in 3.2 ms, including sensor and actuator linearization. The object code for the dynamic control occupies less than 6 Kb of memory. The second processor handles parameter input from a keypad and output to a liquid crystal

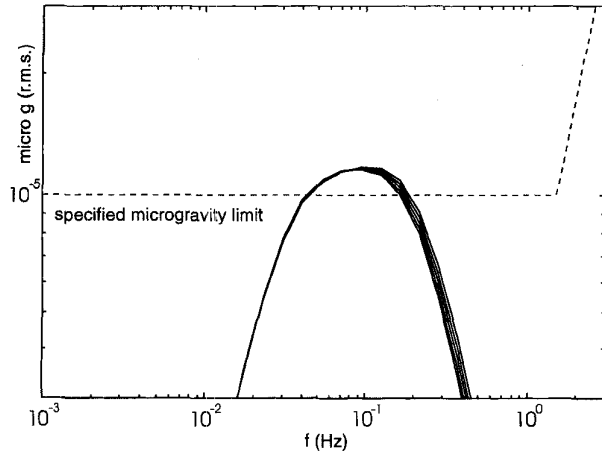


Fig. 13. Predicted acceleration at corner of platform with rotational control.

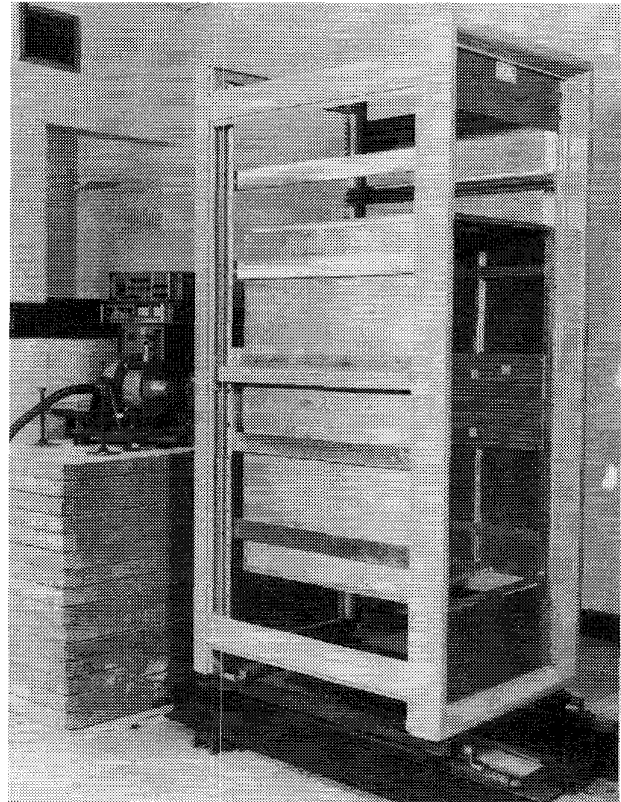


Fig. 14. Photograph of laboratory test rig showing rack unit with liner inside and shaker (on left).

display. It occupies about 17 Kb of memory, a large part of which is stored text, and cycles in about 300 ms. The system software is outlined in Fig. 17 which shows the top-level processes and their priorities.

Communication between the processes is by message-passing channels defined in the software which are mapped onto the transputers' link hardware. Process synchronization is built in to the occam2 programming language and no operating system is required. The dynamic control process is activated at each sample time and runs at a high priority, accepting

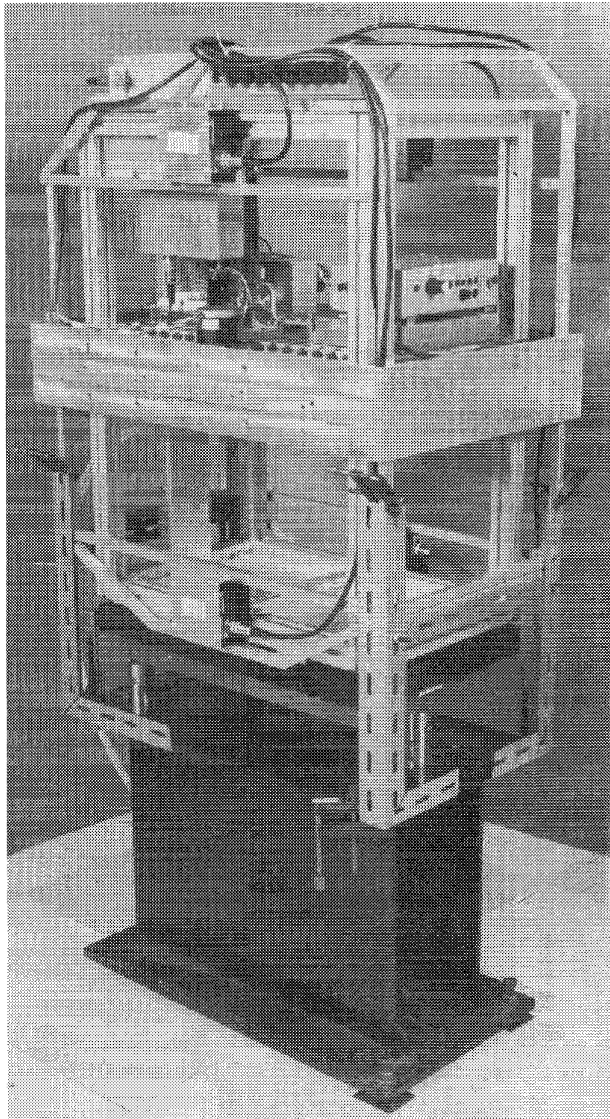


Fig. 15. Photograph of instrumented platform mounted on air table; the central belt locates into the liner unit.

parameter values from the main process and returning values for the measured variables. The communications buffer interposed between the two is always ready to receive messages from either of its communicating sources. The transputer and occam2 were found to be an excellent combination for developing the real-time software.

Acceleration is measured using an inertial navigation grade servo-accelerometer mounted on the platform and transmitting data across the optical link. Relative displacement is obtained from the SAU's, platform displacement relative to the laboratory floor is measured by an auxiliary capacitive sensor and the rack displacement by means of a linear potentiometer.

### C. Test Results

The rack was vibrated in accordance with curve *A* in Fig. 2. Initially, the controller bandwidths for all three DOF's were set at 0.3 Hz, 10 times above the requirement of Fig. 2,

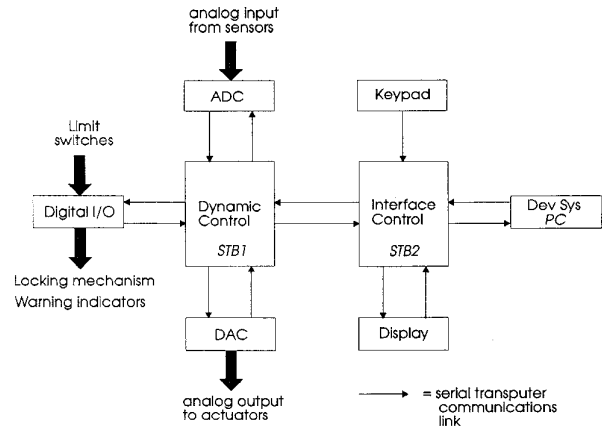


Fig. 16. Digital control system architecture.

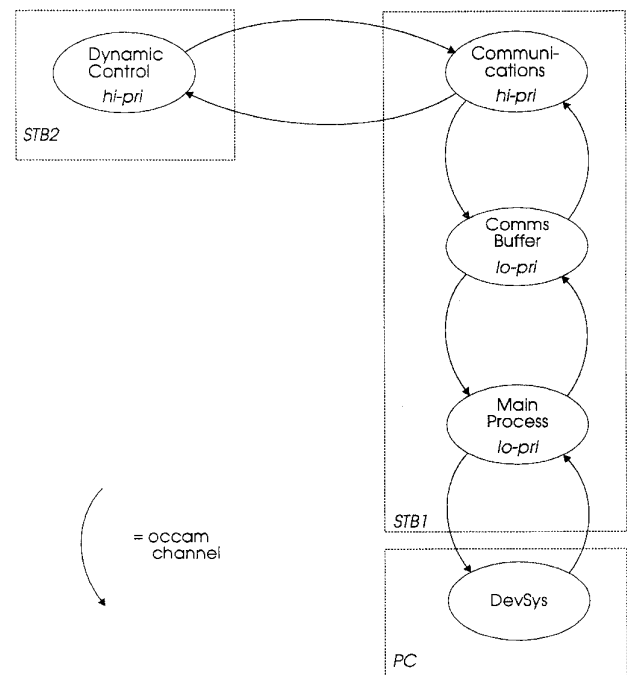


Fig. 17. Top level software structure.

curve *C*. The frequency response of the platform's absolute displacement is shown in Fig. 18 which shows excellent agreement with the model, most experimental points being within 0.5 dB of the predicted response.

Fig. 19 shows the frequency response of the platform's relative displacement (i.e., the air gap) which agrees well with the model (full line,  $k_b = 0$ ) above 0.02 Hz though below this frequency the platform is not tracking the liner motion as well as expected. This set of results demonstrates that the basic isolation characteristic is achieved.

The discrepancy between predicted and measured results becomes more pronounced as the bandwidth of the translation control loop is decreased. Fig. 20 and Fig. 21 show that a large peak at a very low frequency (0.0025 Hz) appears when testing at a system bandwidth of 0.05 Hz, though the high frequency isolation performance is preserved. This effect is

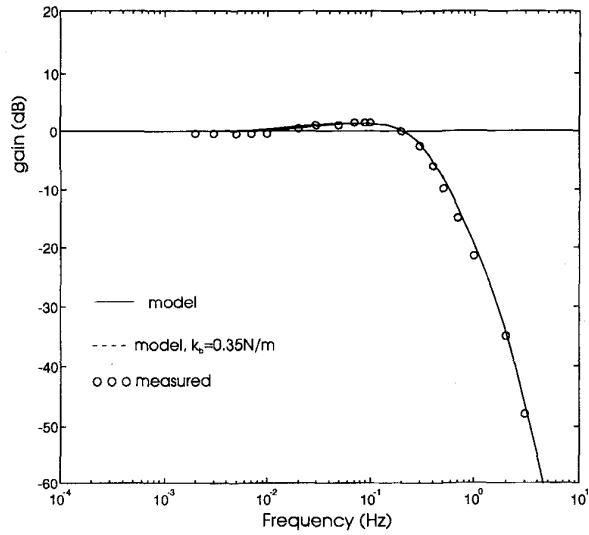


Fig. 18. Frequency response of platform absolute displacement, 0.3 Hz bandwidth.

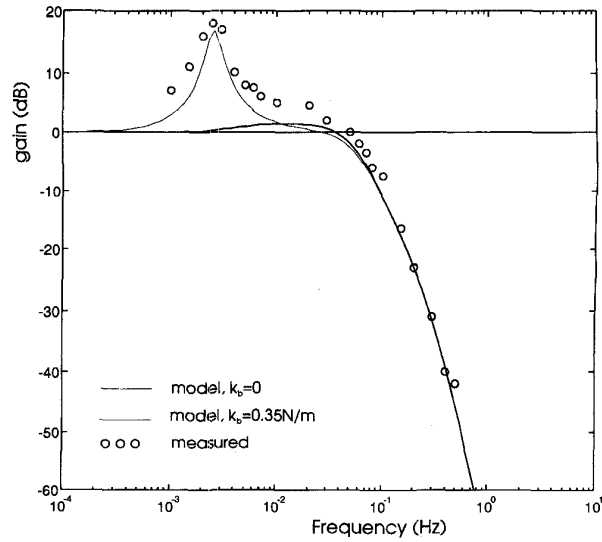


Fig. 20. Frequency response of platform absolute displacement, 0.05 Hz bandwidth.

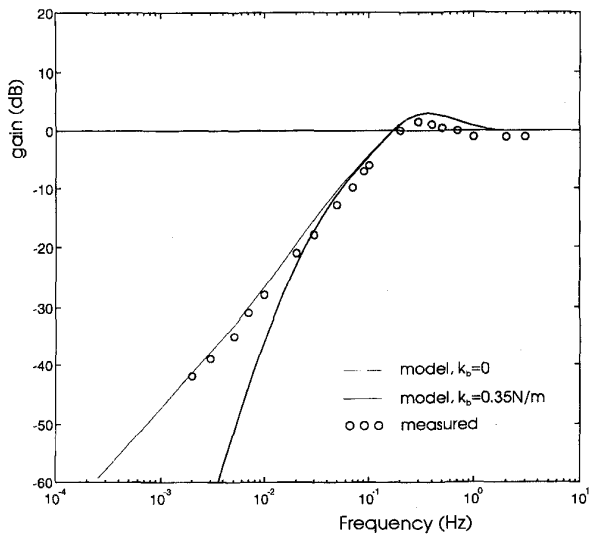


Fig. 19. Frequency response of platform relative displacement, 0.3 Hz bandwidth.

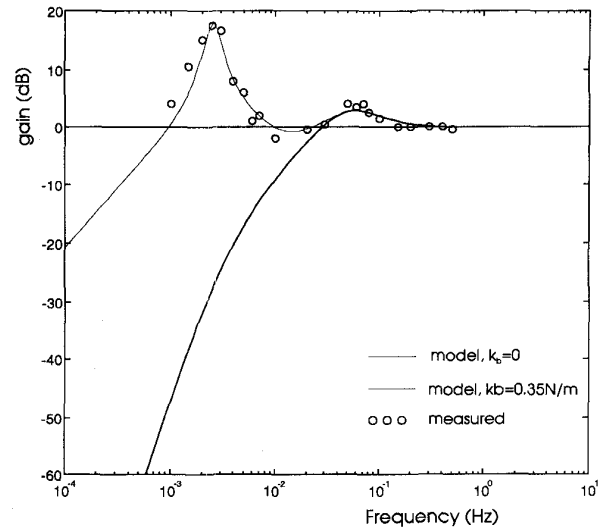


Fig. 21. Frequency response of platform relative displacement, 0.05 Hz bandwidth.

due to the imperfect neutral equilibrium provided by the air table because of the air pressure profile being not quite flat and/or a slight curvature of the table or plate. As shown in Fig. 22, this contributes an “inverted pendulum” force whose magnitude is

$$F_p = \frac{mgy}{r} = k_b y \quad (20)$$

where:

- $F_p$  is the pendulum force;
- $m$  is the platform mass;
- $y$  is the platform displacement;
- $r$  is the effective radius of curvature;
- $k_b$  is an effective stiffness,  $k_b = mg/r$ .

The effective stiffness,  $k_b$ , can be included in the model of Fig. 10 as positive feedback from the output position to

the platform mass. An empirically determined value of  $k_b = 0.35 \text{ N/m}$  (corresponding to an effective radius of curvature of the air table surface of 1500 m) yields excellent agreement with the measured results, as shown by the broken line in Figs. 18–21. We may therefore be confident that this is an artefact of the experiment rather than an inherent property of the MGIM or controller dynamics and that the required isolation characteristic would be obtained under orbital conditions where (apart from the disturbances described in Section II-A) a neutral equilibrium is known to exist.

## VI. CONCLUSIONS

In this paper we have described the development of a control strategy for a microgravity isolation mount which is insensitive to asymmetric distribution of the payload mass,

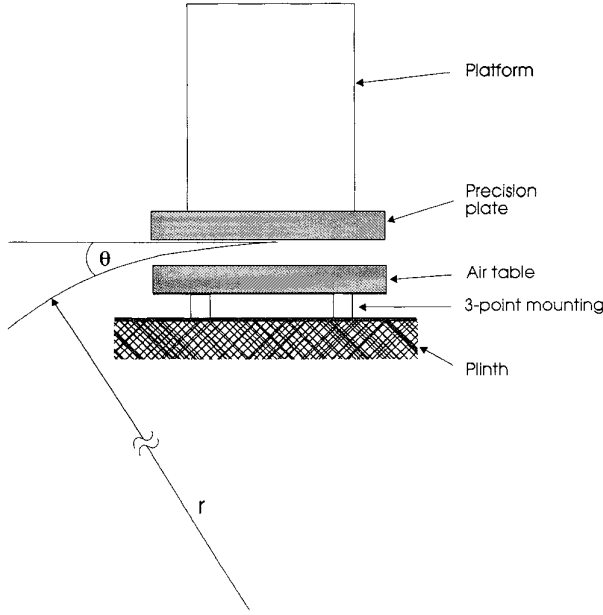


Fig. 22. Illustration of imperfect neutral equilibrium provided by the air table.

making it suitable for a number of different experiment types. The strategy is based on noncontact technology and we have demonstrated how electrical power transfer, heat dissipation, and data transmission can be implemented with extremely low disturbance forces. The results from a laboratory test rig verify the MGIM's vibration isolation performance.

It is clear that measuring the isolation characteristic down to the nominal bandwidth of 0.03 Hz is very difficult in a terrestrial laboratory. Despite the procurement of a custom made air table with vacuum compensation, the effect of tiny deviations from a neutral equilibrium was very noticeable. It is likely that satisfactory elimination of the earth's gravity would require a further independent active control loop with the sole objective of compensating for the inherent positive stiffness of the air table, as used for test and calibration of extremely high sensitivity accelerometers [24]. This was beyond the budget and timescale of our investigation. Extensive computer simulation has shown that it is possible to release and capture the platform successfully by means of a motorized locking mechanism, even in the presence of substantial vibration of the liner. This has been confirmed experimentally. The effect of air trapped between the interleaved cooling fins on the platform and liner has also been considered [25]. Theoretical expressions have been developed for the force caused by air motion and confirmed by measurement on specially constructed fin assemblies. Computer simulation has shown that there is a trade-off between the heat dissipation capacity of the thermal subsystem and the achievable microgravity level, the available gap between platform and liner being a crucial design factor. In turn, this affects the size of the SAU's, the signal strength required at the optical link and the efficiency of the noncontact transformer. This emphasizes that there exists a complex trade-off between the MGIM subsystems and that the control system cannot be designed in isolation.

Following the work described here, further studies performed by ALCA TEL Espace [26] and Deutsche Aerospace [27] have defined detailed engineering models of the MGIM, tailored for use in both Spacelab and the International Space Station.

#### APPENDIX EXPRESSION FOR PLATFORM DISPLACEMENT AND ACCELERATION

From Fig. 10, the state-space models for the platform and controller are

$$\begin{aligned}\dot{\mathbf{x}}_p &= A_p \mathbf{x}_p + B_p \ddot{\mathbf{x}}_p \\ \mathbf{y}_p &= C_p \mathbf{x}_p\end{aligned}\quad (\text{A1})$$

$$\begin{aligned}\dot{\mathbf{x}}_c &= A_c \mathbf{x}_c + B_c \hat{\mathbf{x}}_p \\ \hat{\mathbf{F}}_p &= C_c \mathbf{x}_c + D_c \hat{\mathbf{x}}_p.\end{aligned}\quad (\text{A2})$$

Also from Fig. 10

$$\ddot{\mathbf{x}}_p = M^{-1} C \hat{C}^{-1} \hat{\mathbf{F}}_p \quad (\text{A3})$$

$$\hat{\mathbf{x}}_p = \hat{S}^{-1} S(\mathbf{x}_i - C_p \mathbf{x}_p). \quad (\text{A4})$$

Substituting (A3) into (A1) and (A4) into (A2), respectively, we obtain

$$\begin{aligned}\dot{\mathbf{x}}_p &= A_p \mathbf{x}_p + B_p M^{-1} C \hat{C}^{-1} \hat{\mathbf{F}}_p \\ \mathbf{y}_p &= C_p \mathbf{x}_p\end{aligned}\quad (\text{A5})$$

and

$$\begin{aligned}\dot{\mathbf{x}}_c &= A_c \mathbf{x}_c + B_c \hat{\mathbf{x}}_p \\ \hat{\mathbf{F}}_p &= C_c \mathbf{x}_c + D_c \hat{S}^{-1} S(\mathbf{x}_i - C_p \mathbf{x}_p).\end{aligned}\quad (\text{A6})$$

Combining (A5) and (A6)

$$\dot{\mathbf{x}}_p = A_p \mathbf{x}_p + B_p M^{-1} C \hat{C}^{-1} [C_c \mathbf{x}_c + D_c \hat{S}^{-1} S(\mathbf{x}_i - C_p \mathbf{x}_p)] \quad (\text{A7})$$

$$\dot{\mathbf{x}}_c = A_c \mathbf{x}_c + B_c \hat{S}^{-1} S(\mathbf{x}_i - C_p \mathbf{x}_p). \quad (\text{A8})$$

Expanding and gathering terms in (A7) and (A8) yields the platform and controller states as a function of the input vibration  $\mathbf{x}_i$

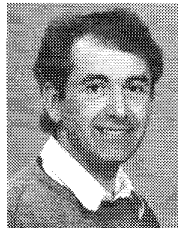
$$\begin{aligned}\begin{bmatrix} \dot{\mathbf{x}}_p \\ \dot{\mathbf{x}}_c \end{bmatrix} &= \begin{bmatrix} A_p - B_p M^{-1} C \hat{C}^{-1} D_c \hat{S}^{-1} S C_p & B_p M^{-1} C \hat{C}^{-1} C_c \\ -B_c \hat{S}^{-1} S C_p & A_c \end{bmatrix} \\ &\cdot \begin{bmatrix} \mathbf{x}_p \\ \mathbf{x}_c \end{bmatrix} + \begin{bmatrix} B_p M^{-1} C \hat{C}^{-1} D_c \hat{S}^{-1} S \\ B_c \hat{S}^{-1} S \end{bmatrix} \mathbf{x}_i\end{aligned}\quad (\text{A9})$$

and the platform accelerations as

$$\ddot{\mathbf{x}}_p = M^{-1} C \hat{C}^{-1} [D_c \hat{S}^{-1} S(\mathbf{x}_i - C_p \mathbf{x}_p) + C_c \mathbf{x}_c]. \quad (\text{A10})$$

## REFERENCES

- [1] D. I. Jones, "Vibration control in space," *IEE Comput. Contr. Eng. J.*, vol. 5, no. 2, pp. 89-95, Apr. 1994.
- [2] D. B. DeBra, "Disturbance compensation system design," *APL Tech. Digest*, vol. 12, no. 2, pp. 14-26.
- [3] R. E. Olsen and J. Mockovciak, "Operational factors affecting microgravity levels in orbit," *J. Spacecraft*, vol. 18, no. 2, pp. 141-144, 1981.
- [4] H. Hamacher and U. Merbold, "Microgravity environment of the material science double rack on Spacelab-1," *J. Spacecraft*, vol. 24, pp. 264-269, May/June 1987.
- [5] J. N. Schoess, D. Thomas, and B. Dunbar, "Measuring acceleration in a microgravity environment," *Sensors*, vol. 7, no. 11, Oct. 1990.
- [6] C. Tiby and D. Langbein, *Allowable g-levels for microgravity payloads*, Battelle Institute, Frankfurt, Germany, European Space Agency Contractor's Rep. 5504/83, 1985.
- [7] A. Sharpe, *Low acceleration characterization of Space Station environment*, Teledyne Brown Eng., Huntsville, AL, Rep. NASA Contract NAS8-36122, 1985.
- [8] F. O. Von Bun and O. K. Garriott, "Nano-g environment on the Orbiter or Space Station," *Acta Astronautica*, vol. 17(5), pp. 579-583, 1988.
- [9] B. J. Hamilton, "Vibration attenuation using magnetic suspension isolation," in *Proc. Joint Amer. Contr. Conf.*, Charlottesville, VA, 1981.
- [10] D. D. Havenhill and K. D. Krall, "Payload isolation using magnetic suspension," in *Proc. Annu. Rocky Mountain Guidance Contr. Conf.*, Keystone, CO, 1985, AAS-85-013.
- [11] R. C. Fenn *et al.*, "An active magnetic suspension for space-based microgravity vibration isolation," in *Proc. Amer. Soc. Mech. Eng. Conf. Active Noise Vibration Contr.*, Dallas, TX, 1990, pp. 49-56.
- [12] L. Germann and A. Gupta, "Active isolation systems," in *Proc SPIE Int. Conf. Space Guidance, Contr., Tracking*, vol. 1949, Orlando, FL, Apr. 1993, pp. 37-42.
- [13] C. M. Grodinsky and K. A. Logsdon, "Development and design of a magnetic inertially referenced isolation system for microgravity experimentation," in *Proc. Wkshp. Aerospace Applicat. Magnetic Suspension Technol.*, Hampton, VA, 1990.
- [14] D. S. Stampleman and A. H. von Flotow, "Microgravity isolation mount based upon piezoelectric film," in *Proc. Amer. Soc. Mech. Eng. Conf. Active Noise Vibration Contr.*, Dallas, TX, 1990, pp. 57-65.
- [15] Z. J. Geng and L. S. Haynes, "Six degree of freedom active vibration control using the Stewart platforms," *IEEE Trans. Contr. Syst. Technol.*, vol. 2, no. 1, pp. 45-53, 1994.
- [16] D. I. Jones, "Strategies for controlling a microgravity isolation mount," in *Proc. Amer. Contr. Conf.*, San Diego, CA, 1990, pp. 2601-2606.
- [17] T. S. Allen, D. D. Havenhill, K. K. Kral, "FEAMIS: a magnetically suspended isolation system for space-based materials processing," in *Proc. Annu. AAS Guidance Contr. Conf.*, Keystone, CO, 1986.
- [18] R. G. Owen *et al.*, "Integration of a microgravity isolation mount (MGIM) within a Columbus single rack," *Acta Astronautica*, vol. 22, pp. 119-128, 1990.
- [19] R. G. Owen, D. I. Jones, and A. R. Owens, "Mechanical design and simulation of a microgravity isolation mount for Columbus," *AIAA J. Spacecraft Rockets*, vol. 30, no. 4, pp. 502-508, 1993.
- [20] D. I. Jones, A. R. Owens, R. G. Owen, G. Roberts, and P. Hadfield, "Microgravity Isolation Mount," Univ. Wales, Bangor, European Space Agency Contractor's Rep. 7637/88, 1991.
- [21] R. G. Owen *et al.*, "Progress in the design and development of a microgravity isolation mount for Columbus," in *Proc 42nd Congr. Int. Astronautical Federation*, IAF-91-379, Montreal, Quebec, Canada, 1991.
- [22] "Spacelab Payload Accommodation Handbook," SLP/2104, Issue 2, NASA Marshall Space Flight Centre, 1985.
- [23] D. I. Jones, A. R. Owens, and R. G. Owen, "A microgravity facility for in-orbit experiments," in *Proc. Amer. Soc. Mech. Eng. Conf. Active Noise Vibration Contr.*, Dallas, TX, 1990, pp. 67-73.
- [24] A. Bernard and P. Touboul, "The GRADIO accelerometer: design and development status," *Proc. ESA/NASA Wkshp. Solid-Earth Mission Aristoteles*, Anacapri, Italy, Sept. 1991.
- [25] D. I. Jones and M. H. Lorenz, "The effect of air motion on a microgravity isolation system," in *Proc SPIE Int. Conf. Space Guidance, Contr., Tracking*, vol. 1949, Orlando, FL, Apr. 1993, pp. 43-53.
- [26] J. P. Provenzano and E. Muller, "The microgravity isolation mount," in *Proc. 1st Space Microdynamics Accurate and Contr. Symp.*, Nice, France, Nov. 1992.
- [27] M. Zier, "The microgravity isolation mount—a Spacelab/Columbus facility to support sensitive experiments," in *Proc. 1st Space Microdynamics and Accurate Contr. Symp.*, Nice, France, Nov. 1992.



**Dewi I. Jones** (M'94) received the B.Sc. degree in electronic engineering from the University of Wales, Bangor, in 1972, and the M.Sc. and Ph.D. degrees in control engineering from the same university.

He was an Ionosphericist with the British Antarctic Survey for three years. Following a two-year period as a Research Engineer with GEC Marconi, he was appointed to a lectureship at the University of Wales, Bangor, in 1980. His present position is Senior Lecturer in the same department, but he is currently with E.A. Technology Ltd. as a Royal Society Industry Fellow. His research interests include parallel processing for real-time control, computation of robot algorithms, and vibration isolation.

Dr. Jones is a Chartered Engineer and Fellow of the Institution of Electrical Engineers.



**A. R. Owens** received the B.Sc. degree in electrical engineering from the University of Wales, Bangor, in 1952 and the M.Sc. degree from the University of Manchester in 1954.

He joined the United Kingdom Atomic Energy Authority, Harwell, in 1955. In 1960 he joined the University of Wales, Bangor where he has recently relinquished the post of Head of the School of Electronic Engineering and Computer Systems. He is active in the fields of nucleonic instrumentation and Space Instrumentation and has spent sabbatical years at Hewlett Packard Research Ltd. in 1977 to 1978 and the Nuclear Physics Group, UKAEA, Harwell, in 1986 to 1987. He will soon spend part of a sabbatical year at the European Synchrotron Radiation Facility, Grenoble, France, as a Visiting Scientist and Consultant. His research interests include the application of DSP techniques to high-rate pulse spectroscopy and design of very fast charge amplifiers for nucleonic applications, design of specialized noncontact power supplies for space applications and stochastic identification techniques.

Mr. Owens is a Chartered Engineer and Member of the Institution of Electrical Engineers.



**R. Gareth Owen** received the B.Sc. degree in engineering with German from the University of Bath in 1981 after which he joined Zahnraederfabrik Renk A.G. in Augsburg as an Engineer. He completed the Ph.D. degree in control engineering at the University of Wales, Bangor, in 1985. He is now studying for the M.B.A. degree at Sophia Antipolis in France.

He remained at Bangor as a Project Engineer working on microgravity isolation techniques until 1993 when he moved to CARRAR in Paris.

Dr. Owen was awarded a European Space Agency Fellowship and studied high accuracy pointing methods at ESTEC in the Netherlands until 1995. He is a Chartered Engineer and a Member of the Institution of Mechanical Engineers and the American Institute of Aeronautics and Astronautics.